

Di-electron Widths of the Upsilon(1S,2S,3S) Resonances

J. Pivarski,¹ J. R. Patterson,¹ and K. Berkelman¹

(CLEO Collaboration)

¹*F. R. Newman Laboratory for Elementary-Particle Physics, Ithaca, New York 14850-8001*

(Dated: July 11, 2005)

Abstract

We have determined the di-electron widths (Γ_{ee}) of the $\Upsilon(1S)$, $\Upsilon(2S)$, and $\Upsilon(3S)$ to be 1.339 ± 0.009 (*stat*) ± 0.020 (*syst*) keV, $0.618 \pm 0.010 \pm 0.009$ keV, and $0.425 \pm 0.009 \pm 0.006$ keV, respectively. To measure these widths to their 2% precisions, the Cornell Electron Storage Ring scanned the production cross-section lineshapes of the three resonances in e^+e^- collisions, providing the CLEO detector with a total of 0.61 fb^{-1} of lineshape data and 0.76 fb^{-1} below resonance for background subtraction. These measurements are a precise check on lattice QCD calculations for an observable related to f_B .

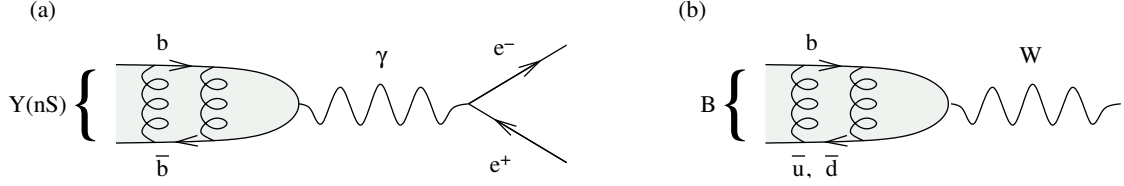


FIG. 1: Feynman diagrams for (a) the process whose probability is measured by Γ_{ee} , (b) the process for f_B .

I. INTRODUCTION

The di-electron width, Γ_{ee} , of $\Upsilon(1S)$, $\Upsilon(2S)$, and $\Upsilon(3S)$ measures the coupling of the $b\bar{b}$ resonance to a two-electron state. In the absence of other Υ decays, Γ_{ee} would be the inverse lifetime of the Υ and the full-width at half-maximum of the Υ 's rest mass distribution. Since Υ does decay to other final states, $\Gamma_{ee} = \mathcal{B}_{ee}\Gamma$, and represents about 1 keV of the Υ 's 50 keV full width. Given \mathcal{B}_{ee} , Γ_{ee} is used to determine Γ .

The $\Upsilon \rightarrow e^+e^-$ process consists of two steps: first the two b quarks must find each other and annihilate, then e^+e^- are produced electromagnetically through a virtual photon (see Figure 1-a). This second step is well-understood QED, and can be used as a probe of the QCD involve in the first. For instance, the $b\bar{b}$ spatial wavefunction, evaluated at the origin, can be calculated from

$$|\psi(0,0,0)|^2 = \left(\frac{3M_\Upsilon^2}{16\pi\alpha_{\text{QED}}^2} \right) \Gamma_{ee} \quad (1)$$

because the two b quarks must fluctuate to the same point in space before annihilation [1]. This gives us some idea of the width of the wavefunction in space, and therefore the strength of the force that binds the two quarks.

Most importantly, Γ_{ee} can test the newly “unquenched” lattice QCD calculations [2] because it can be calculated to high accuracy (2–5%). This anticipated theoretical accuracy is better than the current experimental precision of Γ_{ee} (for the $\Upsilon(2S)$ and $\Upsilon(3S)$ at least), so a new set of high-precision measurements would test the predictive power of the unquenched techniques. Also, notice the similarity of the process measured by Γ_{ee} and that of f_B (Figure 1): the QCD part differs only in the mass of one quark in a central force problem. Verification of the lattice Γ_{ee} calculation would lend credence to a lattice f_B calculation.

II. MEASUREMENT TECHNIQUE, DATASETS, AND DETECTOR

Perhaps surprisingly, Γ_{ee} is not measured by observing $\Upsilon \rightarrow e^+e^-$, but by observing $e^+e^- \rightarrow \Upsilon$. This is because the 50 keV full width is too narrow to be measured directly, and $\Upsilon \rightarrow e^+e^-$ can only be used to get \mathcal{B}_{ee} . The production process, $e^+e^- \rightarrow \Upsilon$, is related to the decay by time-reversal symmetry, provided we integrate over initial-state e^+e^- energies.

$$\Gamma_{ee} = \frac{M_\Upsilon^2}{6\pi^2} \int \sigma(e^+e^- \rightarrow \Upsilon) dE, \quad (2)$$

where σ is the production cross-section [3] [1].

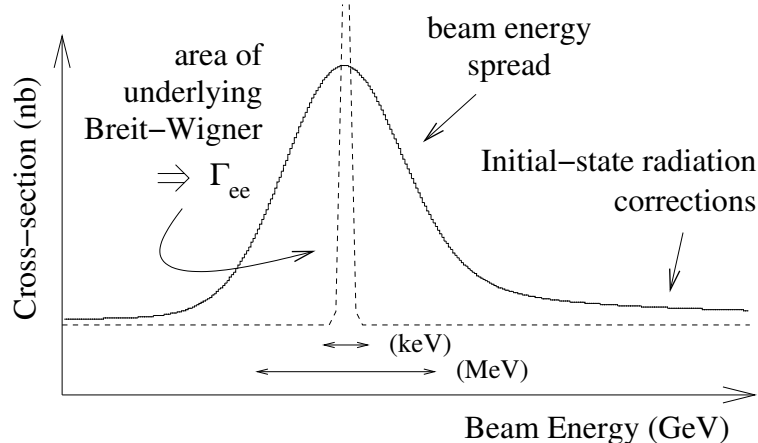


FIG. 2: A cartoon of the Γ_{ee} measurement: we observe the shape of the Breit-Wigner, Gaussian, ISR tail convolution in cross-section versus beam energy and fit for the area of the Breit-Wigner.

We measure the Υ production cross-section at the Cornell Electron Storage Ring (CESR) as a function of incident beam energy (a tunable parameter), and call this distribution the lineshape. (It is a spectral line in analogy with the short-lived excited states of hydrogen.) The area under this lineshape, if it were a pure Breit-Wigner resonance, is the integral needed by Equation 2. The energy spread of the e^+e^- is 0.04% of the beam energy, or about 4 MeV near the Υ mass, and this convolves the Breit-Wigner with a Gaussian that obscures its natural width but preserves its area exactly. Another complication is that high-energy e^+e^- beams can radiate a photon before colliding, reducing their energy to the Υ mass-energy, and then produce an Υ state. This raises the cross-section on the high-energy side of the resonance peak. This (divergent) high-energy tail should not be included in the integral, so Γ_{ee} is measured by fitting the observed lineshape to a three-way convolution of Breit-Wigner, Gaussian, and initial-state radiation tail (calculated by Kuraev and Fadin [4]) [5] with the Breit-Wigner area as a floating parameter (see Figure 2).

CESR devoted 0.10 fb^{-1} , 0.06 fb^{-1} , and 0.10 fb^{-1} to scans of the $\Upsilon(1S)$, $\Upsilon(2S)$, and $\Upsilon(3S)$ lineshapes between November 2001 and August 2002. Each resonance was scanned once a week, and each weekly scan covered the entire resonance to be able to act as an independent measurement of Γ_{ee} . This is because we were wanted to minimize sensitivity to weekly shifts in beam energy calibration: the beam energy is measured with an NMR probe in a test magnet in series with the ring magnets, and it may be displaced by machine studies.

In addition to the dedicated scan data, we included general-purpose off-resonance and on-resonance data as points in the lineshape. Off-resonance data were collected about 20 MeV below each resonance (0.18 fb^{-1} , 0.44 fb^{-1} , and 0.16 fb^{-1}), which is far enough from the resonance that they are insensitive to weekly shifts in beam energy. The off-resonance data have been combined into three cross-section measurements, one for each resonance. On-resonance data are sensitive to beam energy fluctuations, so only data within 48 hours of a scan are used (0.17 fb^{-1} , 0.03 fb^{-1} , 0.15 fb^{-1}).

The Υ cross-section was measured at each energy point by CLEO, a nearly 4π general-purpose detector built around the CESR collision point [6]. This analysis only made use of the central drift chamber and inner silicon vertex detector for charged particle tracking (in

a solenoidal magnetic field) and the CsI crystal calorimeter for measuring the energies and trajectories of neutral particles. The CLEO trigger accepts events that have a minimum number of trigger tracks (AXIAL if observed in the first 16 drift chamber layers, STEREO if extended into the remaining 31) and calorimeter clusters (CBLO if a calorimeter tile measures more than 150 MeV, CBMD if 750 MeV, and CBHI if 1.5 GeV). Our analysis trigger accepts events with at least

$$\begin{aligned} & (3 \text{ AXIAL and } 1 \text{ CBLO}) \text{ or} \\ & \quad (2 \text{ STEREO and } (2 \text{ CBLO or } 1 \text{ CBMD})) \text{ or} \\ & \quad (1 \text{ AXIAL and } 1 \text{ CBMD}). \end{aligned} \quad (3)$$

We will also make use of a two-track trigger (2 AXIAL tracks, prescaled by a factor of 20) and a Gamgam trigger (2 CBHI on opposite sides of the calorimeter barrel) for $e^+e^- \rightarrow \gamma\gamma$.

CLEO data were taken in one-hour runs that correspond to fills of the electron storage ring. About 2% of the relevant runs were excluded because of trigger and event selection inefficiencies peculiar to these runs.

The detector is simulated with a Monte Carlo based on GEANT [7], with Υ events generated by EvtGen [8], which calls JetSet 7.4 [9] for hadronization.

III. CROSS-SECTION MEASUREMENT

The central objective of this analysis is to produce a plot of Υ cross-section versus energy, which can be fitted for Γ_{ee} . We will first establish a set of selection criteria (“cuts”) which define a sample of Υ decays, and estimate the number of false positives in this sample. Having subtracted these backgrounds from our Υ count, we will then consider the inverse problem: how many Υ events were left out. This can be determined directly for $\Upsilon(1S)$ events, as the decay $\Upsilon(2S) \rightarrow \pi^+\pi^-\Upsilon(1S)$ provides two charged tracks ($\pi^+\pi^-$) which can be used to identify the event with little ambiguity. From this second, unbiased sample, we count the fraction of $\Upsilon(1S)$ events which satisfy our cuts, thus measuring the cuts’ efficiency for $\Upsilon(1S)$ decays without assuming a set of decay modes. The more energetic states, $\Upsilon(2S)$ and $\Upsilon(3S)$, can decay the same ways as the $\Upsilon(1S)$, but can additionally cascade to lower-energy $b\bar{b}$ bound states (such as $\Upsilon(1S)$ or $\chi_b(1P)$) before the b quarks annihilate. This adds a correction to the $\Upsilon(2S)$ and $\Upsilon(3S)$ efficiencies, but it can be simulated with Monte Carlo.

Then we will have a true number of $e^+e^- \rightarrow \Upsilon$ events, but this is a function of the luminosity of the e^+e^- beams and the length of time we collected data. We therefore divide by the time-integrated luminosity to obtain a cross-section. We determine the integrated luminosity of a given run by counting a subset of “Gamgam” ($e^+e^- \rightarrow \gamma\gamma$) events in that run and normalizing this count to the known integrated luminosity of the off-resonance data. The Gamgam event type is strictly proportional to integrated luminosity because it has negligible background from Υ decays, as Υ and $\gamma\gamma$ have incompatible C-parity.

A. Selection Criteria and Backgrounds

To suppress large continuum backgrounds such as Bhabhas ($e^+e^- \rightarrow e^+e^-$), we select only hadronic events, that is, all Υ decays except $\Upsilon \rightarrow e^+e^-$, $\Upsilon \rightarrow \mu^+\mu^-$, and $\Upsilon \rightarrow \tau^+\tau^-$. The Υ efficiency then consists of two factors: the efficiency of hadronic decays and $1/(1 - 3\mathcal{B}_{\mu\mu})$,

which corrects for the missing leptonic modes by assuming each to have the same branching fraction (Lepton Universality) [3]. We will show that the hadronic efficiency is very high: 96–98% of hadronic Υ decays pass all cuts.

To discriminate against e^+e^- and $\mu^+\mu^-$ final states, which usually generate two beam-energy tracks, we require the largest track momentum ($\times c$) to be less than 80% of the beam energy. This cut eliminates over 99% of e^+e^- and $\mu^+\mu^-$. The remaining Bhabha background, along with continuum hadrons ($e^+e^- \rightarrow q\bar{q}$) which are indistinguishable from hadronic Υ decays, contribute to a flat mesa below the Υ resonance lineshape (see Figure 3). These backgrounds are effectively subtracted by adding a $1/s$ term (s = beam energy squared) to the lineshape fit function and including the off-resonance cross-section measurement as a point in the fit.

Not all backgrounds, however, depend on beam energy as $1/s$. Two-photon fusion, in which the incident e^+e^- do not collide but emit virtual photons which do, depends on beam energy as $\log s$. Most of these events have low visible energy, the sum of all charged particle energies (measured by their track momenta, assuming pion masses) and neutral particle energies (measured by calorimeter showers that cannot be matched to any charged tracks). Two-photon fusion events usually generate little visible energy in the detector because much of the initial state energy is carried down the beampipe by one or both of the incident beams that failed to collide. We only accept events in which more than 40% of the center-of-mass energy is visible. This cut eliminates most of the two-photon events, which peak below 20% (see Figure 4). We gauge the fraction of two-photon events that survive this cut by fitting the three off-resonance data points for deviations from $1/s$: correcting for high-energy tails from $\Upsilon(1S)$ and $\Upsilon(2S)$, the fraction of two-photon events at 9 GeV returned by the fit is $(8.0 \pm 0.5)\%$ (see Figure 5). This 8% may include other non- $1/s$ contributions (such as J/ψ tails, variation in continuum cut efficiency, or variation in R), but we only need to know the shape of the background for the lineshape fits, not its exact composition.

This visible energy cut also rejects some $\tau^+\tau^-$ events, as these subsequently decay into final states involving neutrinos. However, 58% remain after cuts, and this background is seemingly irreducible as the final states look like hadronic events: they have two or more low-momentum tracks without strong geometric correlations. They are therefore allowed to contribute to $0.58 \times \mathcal{B}_{\tau\tau} \approx 1\%$ of the resonance peak.

Any backgrounds which vary slowly with beam energy and are proportional to luminosity can be subsumed into the fit parameters described above. Cosmic rays, however, will not be proportional to luminosity as they come from an external source. We reject most cosmic rays by requiring that the distance of closest approach of the closest track to the beamline (d_{XY}) be less than 5 mm (a very loose cut: d_{XY} has an RMS of 0.2 mm). We find the number of cosmic rays that survive hadronic cuts by applying the cuts to a control dataset with no beams in CESR (cosmic rays only), normalized by the number of events satisfying special cosmic ray cuts, for each run. Figure 3 shows the result of this measurement for $\Upsilon(3S)$ data (typically 0.4% of the continuum), and Figure 6-a shows d_{XY} for events that passed all other cosmic rays cuts, for experimental and control data.

Another two backgrounds which aren't proportional to luminosity are beam-gas events, in which one beam electron or positron collides with a gas atom inside the beampipe, and beam-wall, in which a beam particle collides with the wall of the beampipe. These are suppressed by calculating an approximate vertex for each event in Z, along the beamline (called d_Z). Beam-gas and beam-wall events may occur anywhere along the beamline, but beam-beam collisions must originate within a few centimeters of the nominal beam spot. We

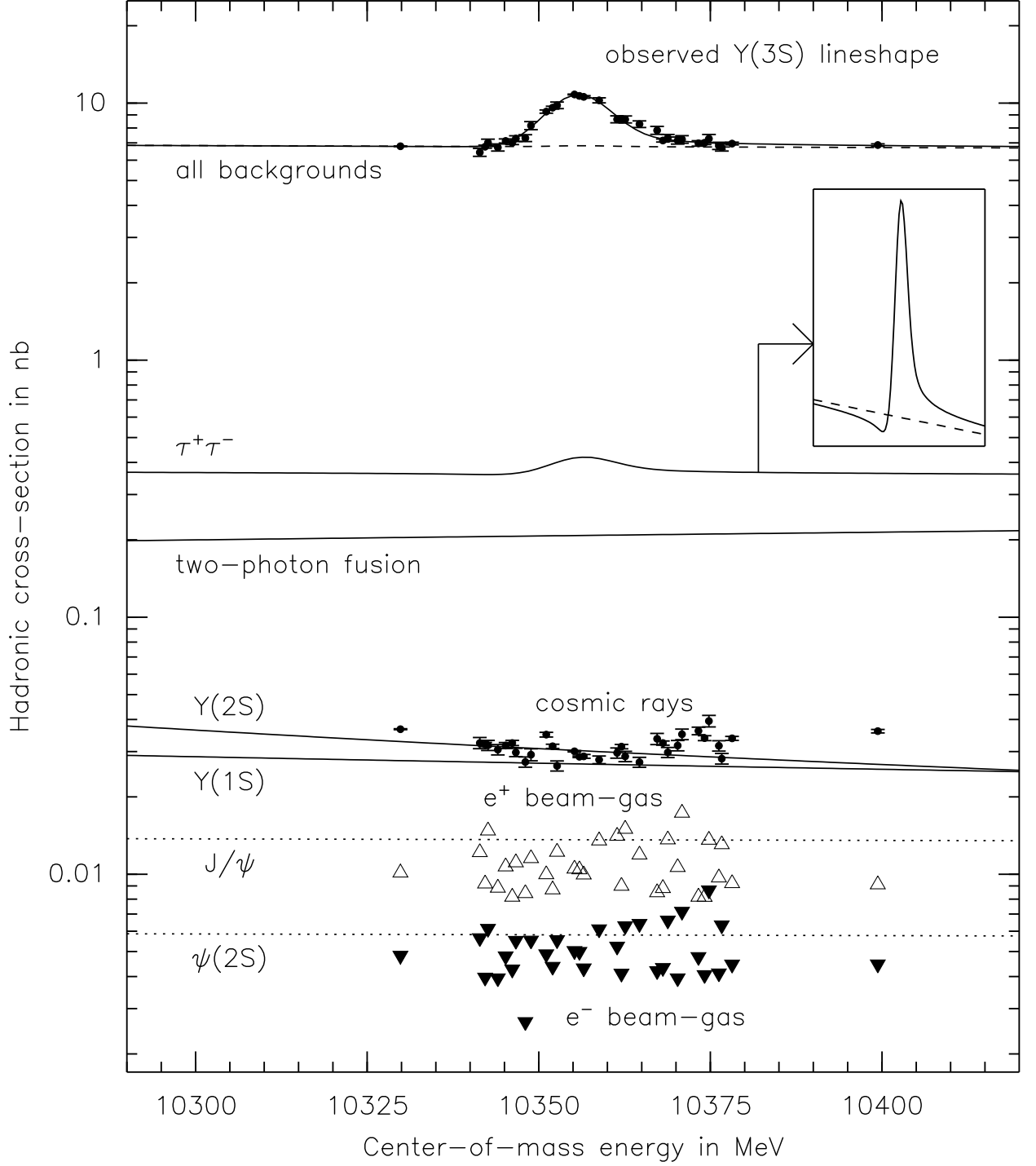


FIG. 3: All $\Upsilon(3S)$ backgrounds ($\Upsilon(1S)$ and $\Upsilon(2S)$ backgrounds are smaller).

Lines, top to bottom: fitted lineshape, all backgrounds (dashed), continuum and resonance $\tau^+\tau^-$, with interference (see inset: dashed is continuum without resonance); two-photon fusion, which rises as $\log s$; $\Upsilon(2S)$ and $\Upsilon(1S)$ high-energy tails, which descend as $1/(E - M_\Upsilon)$; J/ψ and $\psi(2S)$ tails (dotted), which are not corrected for (they contribute to “two-photon”).

Points, top to bottom: observed lineshape, cosmic rays (with statistical uncertainties), positron-induced beam-gas (open triangles), and electron-induced beam-gas (filled triangles).

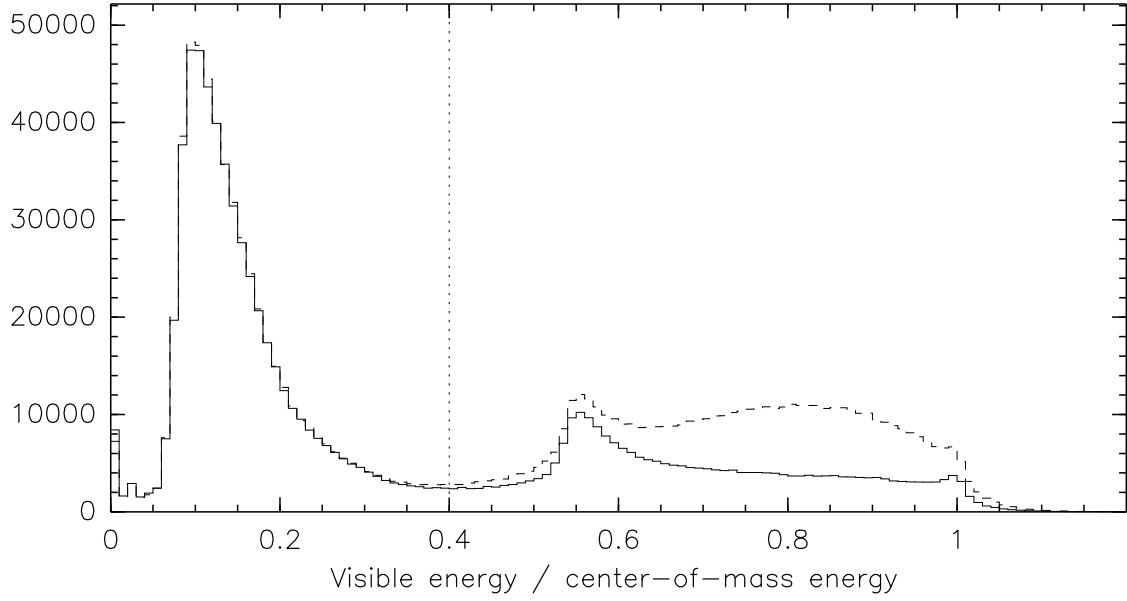


FIG. 4: Visible energy of off-resonance data (solid histogram), showing a large peak of two-photon background below 20% of the center-of-mass energy. The dotted line indicates the cut threshold and the dashed histogram shows Υ events on top of the background (from on-resonance data).

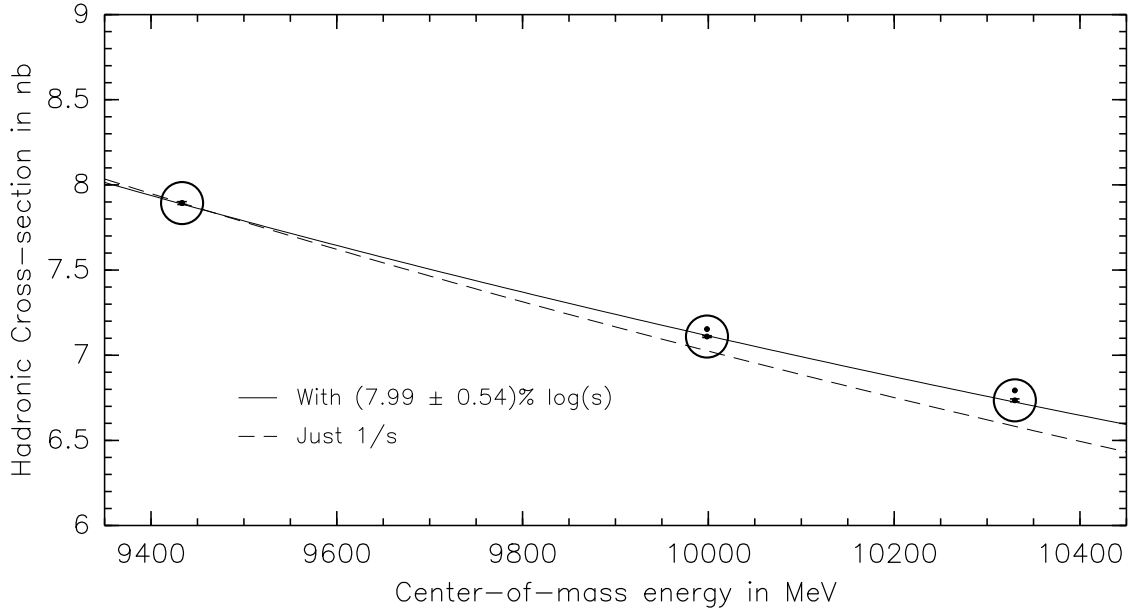


FIG. 5: The three off-resonance points showing $\Upsilon(1S)$ and $\Upsilon(2S)$ tail corrections (corrected points are lower), fitted to $1/s + \log s$ (solid line). The dashed line shows a pure $1/s$ fit through $\Upsilon(1S)$ off-resonance for comparison.

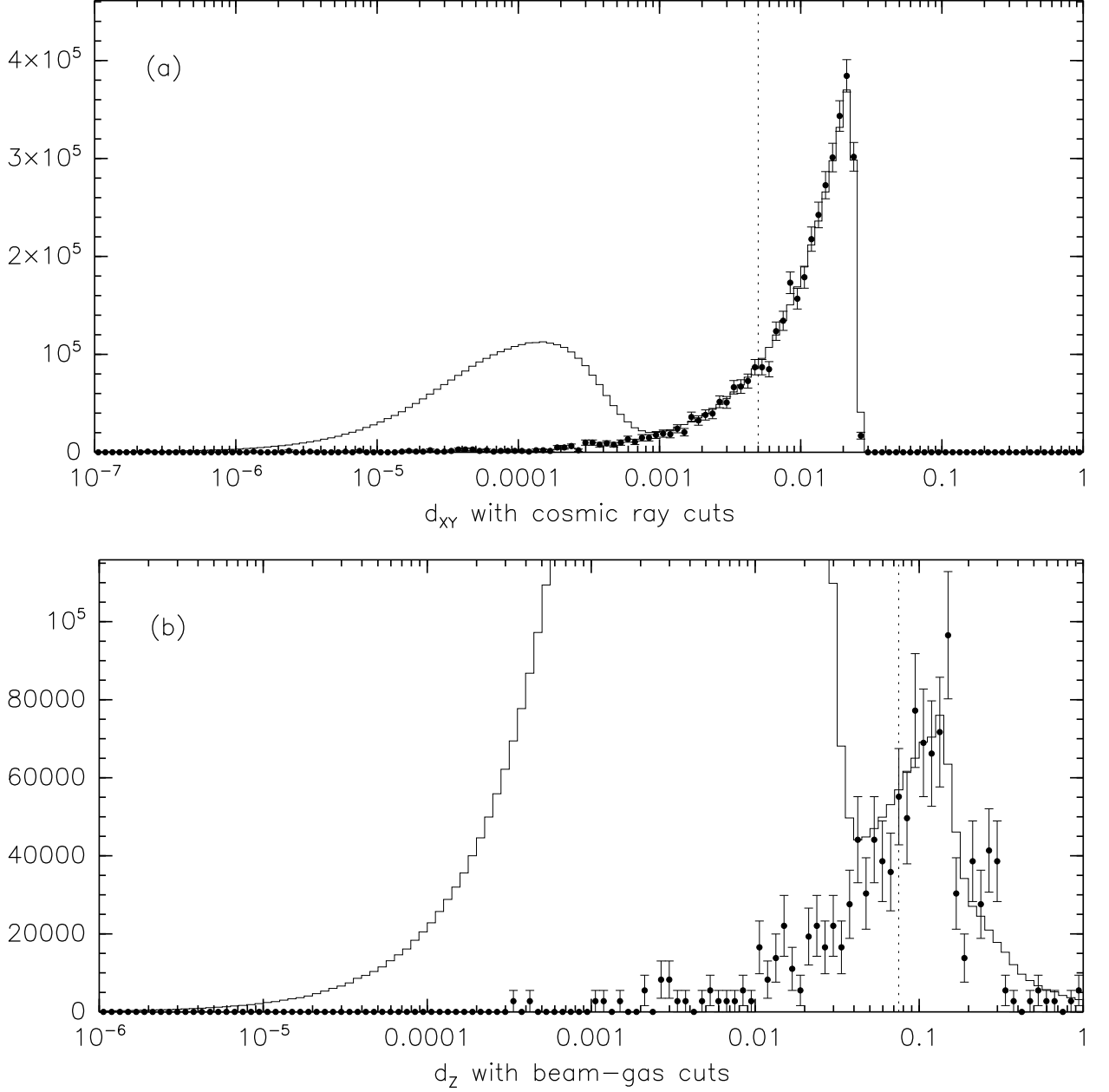


FIG. 6: Two geometric variables used to select cosmic rays and beam-gas. In each case, the histogram is all experimental data, and the points are a control (beamless data or single-beam data).

(a) d_{XY} , the distance of closest approach of the closest track to the beamline, after other cosmic ray cuts (in log x scale: 0.01 is 1 cm). The distribution above 5 mm (dotted line) is well-described by no-beam data.

(b) d_Z , the distance of the event vertex from the nominal beam spot, as measured along the beamline. Although beam-gas cuts reject events with $d_Z < 7.5$ cm (dotted line), the beam-gas count may be contaminated by some collision data.

cut at 7.5 cm (also loose: d_Z has an RMS of 1.5 cm). To count survivors, we construct a set of beam-gas cuts and test them in a single-beam control sample, in analogy to cosmic ray counting above (except that cosmic rays need to be subtracted from the single-beam sample). Figure 6-b shows d_Z after other beam-gas cuts, for experimental and control data. Unlike cosmic rays, which are easily distinguished from collision data and are well-represented by the no-beam sample (6-a), beam-gas cuts before d_Z have a large background from collision data, and the low-precision in the single-beam sample makes it unclear how many collision events have large d_Z . As a precaution, we subtract $50\% \pm 50\%$ of the estimated beam-gas background from our hadronic event count. Beam-wall events were found to be much less common than beam-gas, and are subsumed into this uncertainty. As the e^+ and e^- beams may have different currents, we count electron-induced beam-gas independently of positron-induced beam-gas. (They can be distinguished by their net Z momentum.) Beam-gas counts are also plotted in Figure 3; they typically amount to 0.1% of the continuum.

B. Hadronic Efficiency

Now that we know we can subtract non- Υ events from our hadronic event count (or cover the remainder with an uncertainty), we turn to the issue of hadronic Υ decays missing from that count. These events may be missing because they are detected but fail our four cuts, or, more seriously, because they fail to trigger. For example, the decay $\Upsilon \rightarrow Z^* \rightarrow \nu\bar{\nu}$, which is “hadronic” by our choice of definition, generates no tracks and no showers. We need to put a limit on invisible decays such as this, ideally one that assumes as little as possible from a theoretical model. This limit will dominate the uncertainty in hadronic efficiency.

All $\Upsilon(1S)$ decays can be seen from $\Upsilon(2S) \rightarrow \pi^+\pi^-\Upsilon(1S)$ if the two tracks left by the charged pions are sufficient to satisfy the trigger. A pion with more than 150 MeV of transverse momentum will generate an AXIAL track in the trigger with $(99.93 \pm 0.07)\%$ probability [10]. By requiring both pions to satisfy this criterion and selecting events from the prescaled two-track trigger, we obtain a complete and unbiased set of $\Upsilon(1S)$ decays, though at a cost of a factor of 20 in sample size.

The $\Upsilon(2S) \rightarrow \pi^+\pi^-\Upsilon(1S)$ events in this sample are identified by requiring the recoil mass of the two pions

$$m_{\pi\pi\text{-rec}}^2 = \left(2E_{\text{beam}} - \sqrt{|\vec{p}_1|^2 + m_\pi^2} - \sqrt{|\vec{p}_2|^2 + m_\pi^2}\right)^2 - |\vec{p}_1 + \vec{p}_2|^2 \quad (4)$$

to be close to the $\Upsilon(1S)$ mass. As can be seen in Figure 7-a, the $\Upsilon(1S)$ peak sits on top of a flat background of random two-track combinations, sometimes from true $\Upsilon(2S) \rightarrow \pi^+\pi^-\Upsilon(1S)$ decays but often from other event types. We suppress this combinatoric background by requiring the pair of tracks to intersect near the beam spot and to have opposite charges, but ultimately, the remainder will need to be subtracted by a linear fit.

We first want to learn from this study how many $\Upsilon(1S)$ events are “invisible,” which we will take to mean how many fail to generate one AXIAL track and one CBLO (150 MeV cluster) in the trigger. This is a necessary condition for the analysis trigger, so any event that fails this simple criterion will fail the exact trigger criteria described in Equation 3. We fit the recoil mass peak to a double Gaussian (Figure 7-a) and use the same mean, sigmas, and area ratio in a fit to the invisible events (Figure 7-b). The ratio of these two is $(0.67 \pm$

Criterion	Efficiency
1. Visible to trigger: ≥ 1 AXIAL track and ≥ 1 CBLO (150 MeV cluster)	$(99.22^{+0.48}_{-0.57})\%$
Passed all cuts (assuming visible $\Upsilon(1S)$)	$(92.58 \pm 0.13)\%$
Passed all cuts (assuming visible hadronic $\Upsilon(1S)$)	$(98.32 \pm 0.21)\%$
2. Passed all cuts without boost/track confusion (assuming the above)	$(98.46 \pm 0.30)\%$
3. Passed trigger (Equation 3, assuming visible and passed cuts)	$(99.87 \pm 0.13)\%$
$\Upsilon(1S)$ hadronic efficiency (product of 1, 2, and 3)	$(97.57^{+0.58}_{-0.66})\%$

TABLE I: Summary of cut efficiency measurement for $\Upsilon(1S)$.

0.62)%, so the probability for an $\Upsilon(1S)$ to be “visible to the trigger” is $(99.22^{+0.48}_{-0.57})\%$, after correcting for the fact that efficiencies must be less than 100%.

The hadronic efficiency of our cuts can be more precisely determined because we do not need to use as small a set of $\Upsilon(2S) \rightarrow \pi^+\pi^-\Upsilon(1S)$ events. Instead of only considering events from the prescaled two-track trigger, we can use events from an unprescaled trigger which requires three AXIAL tracks and one CBLO. This sample is called low-bias (see Figure 7-c for a recoil mass plot) because the $\Upsilon(1S)$ must supply one AXIAL track and one CBLO; e.g., it must be “visible.” We apply our hadronic cuts, excluding the two pions, to this sample and count $\#pass/(\#pass + \#fail)$, first subtracting scaled sideband events ($m_{\pi\pi\text{-rec}} \in (9.441, 9.454) \cup (9.472, 9.480)$ GeV) from signal events ($9.454 < m_{\pi\pi\text{-rec}} < 9.472$ GeV). Figure 7-d shows the recoil mass of events that failed the cuts. This fraction, which includes $\Upsilon(1S) \rightarrow e^+e^-$, $\mu^+\mu^-$, and $\tau^+\tau^-$, is $(92.58 \pm 0.13)\%$. Correcting for leptonic modes, the hadronic cut efficiency is $(98.32 \pm 0.21)\%$.

We repeated this procedure for $\Upsilon(2S) \rightarrow \pi^+\pi^-\Upsilon(1S)$ Monte Carlo, and obtained a $(98.54 \pm 0.22)\%$ hadronic cut efficiency, in good agreement with the data. We also simulated $e^+e^- \rightarrow \Upsilon(1S) \rightarrow \text{hadronic modes}$, in which we found a $(98.68 \pm 0.04)\%$ efficiency: also in good agreement. Using the ratio of these Monte Carlo predictions as a 1.0014 ± 0.0022 correction factor, the $e^+e^- \rightarrow \Upsilon(1S)$ hadronic cut efficiency is $(98.46 \pm 0.30)\%$.

Distributions of the four variables used in our cuts are presented in Figure 8, after subtracting combinatoric backgrounds. Monte Carlo ($\Upsilon(2S) \rightarrow \pi^+\pi^-\Upsilon(1S)$) is overlaid for comparison.

In general, our analysis trigger requires more than one AXIAL track and one CBLO. The trigger efficiency, after our “visible to trigger” condition and hadronic cuts, is 99.87% in Monte Carlo. A comparison of AXIAL, STEREO, CBLO, and CBMD distributions in data and Monte Carlo indicate that the simulation can be trusted, at the very least within 100% of the predicted effect (Figure 9), so we will assign it a systematic error of 0.13%.

The $\Upsilon(1S)$ hadronic efficiency is $(97.57^{+0.58}_{-0.66})\%$, the product of these three cumulative efficiencies (listed in Table I).

The $\Upsilon(2S)$ and $\Upsilon(3S)$ can decay into any final states that the $\Upsilon(1S)$ can, but can also cascade into lower $b\bar{b}$ resonances. This has three implications: the 0.7% uncertainty in invisible $\Upsilon(1S)$ decays must be shared by the $\Upsilon(2S)$ and $\Upsilon(3S)$, the efficiency will need to be corrected for cascade decays, and, in particular, for cascades in which a lower Υ decays into e^+e^- or $\mu^+\mu^-$, as these will be lost to our cuts.

We answer the first two considerations by first correcting the $\Upsilon(1S)$ efficiency for all cascade decay modes except “cascades to leptons” (e^+e^- and $\mu^+\mu^-$). Simulations of $e^+e^- \rightarrow$

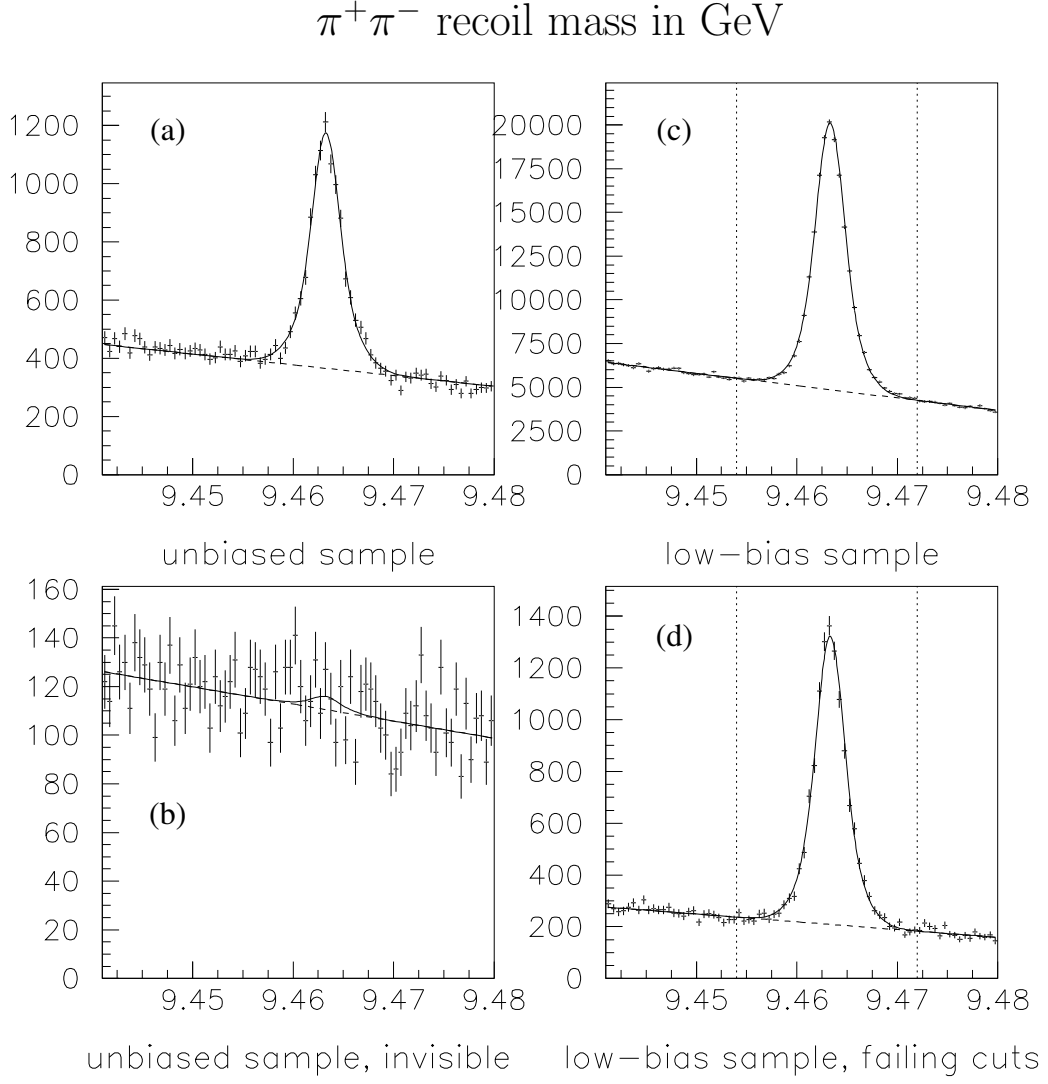


FIG. 7: Recoil mass of $\pi^+\pi^-$ in (a) the unbiased sample (all Υ decays are present), (b) the unbiased sample for invisible decays (no AXIAL tracks or no 150 MeV clusters), (c) the low-bias sample (Υ must be visible), and (d) the low-bias sample failing hadronic cuts. Most of the $\Upsilon(1S)$ decays in (d) are lepton pairs.

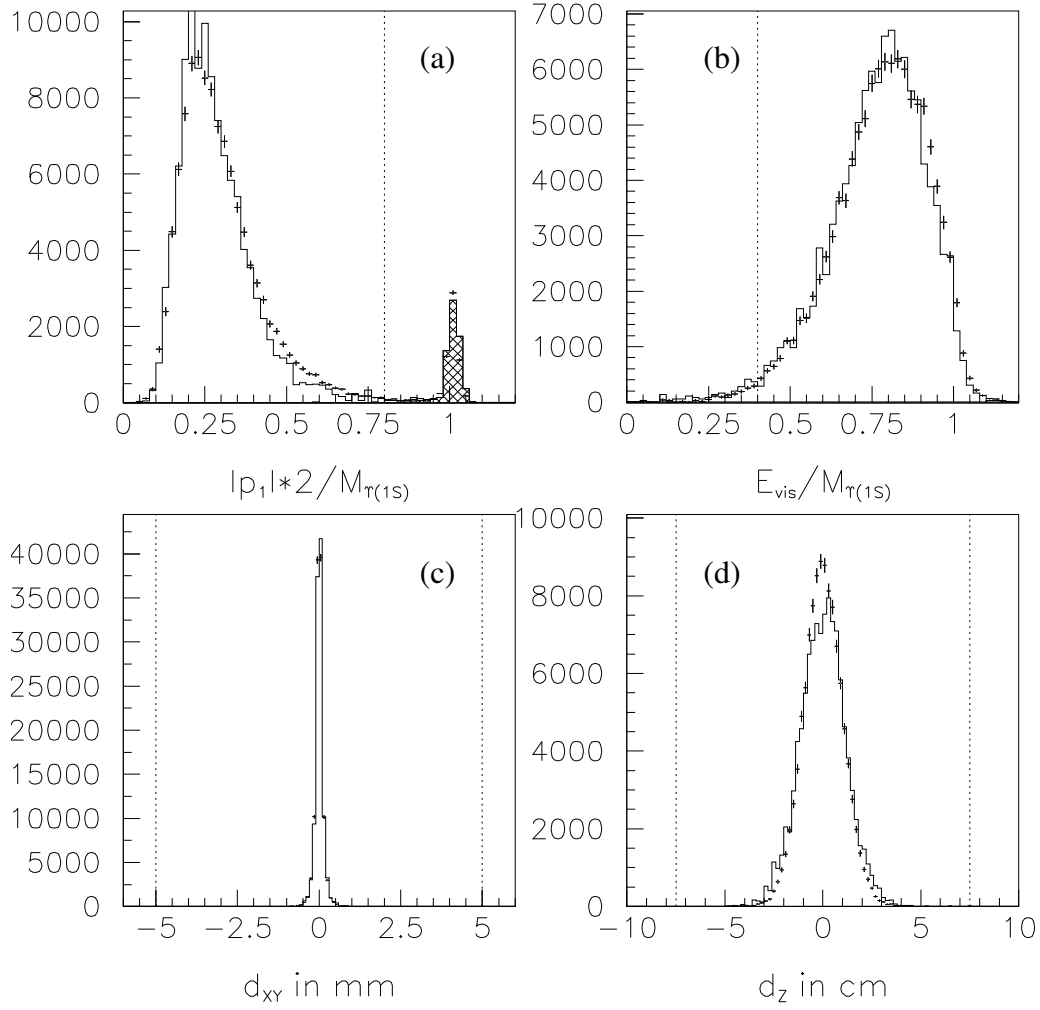


FIG. 8: The four hadronic cuts, as seen in $\Upsilon(2S) \rightarrow \pi^+\pi^-\Upsilon(1S)$ decays. Points are data (with combinatoric backgrounds subtracted) and histograms are Monte Carlo; dotted lines are cut thresholds. (All cuts are applied except the one presented.) (a) Biggest track momentum $< 80\%$ beam energy (cross-hatched histogram is e^+e^- , $\mu^+\mu^-$ Monte Carlo), (b) visible energy $> 40\%$ expected center-of-mass energy, (c) $|d_{XY}| < 5$ mm, and (d) $|d_Z| < 7.5$ cm.

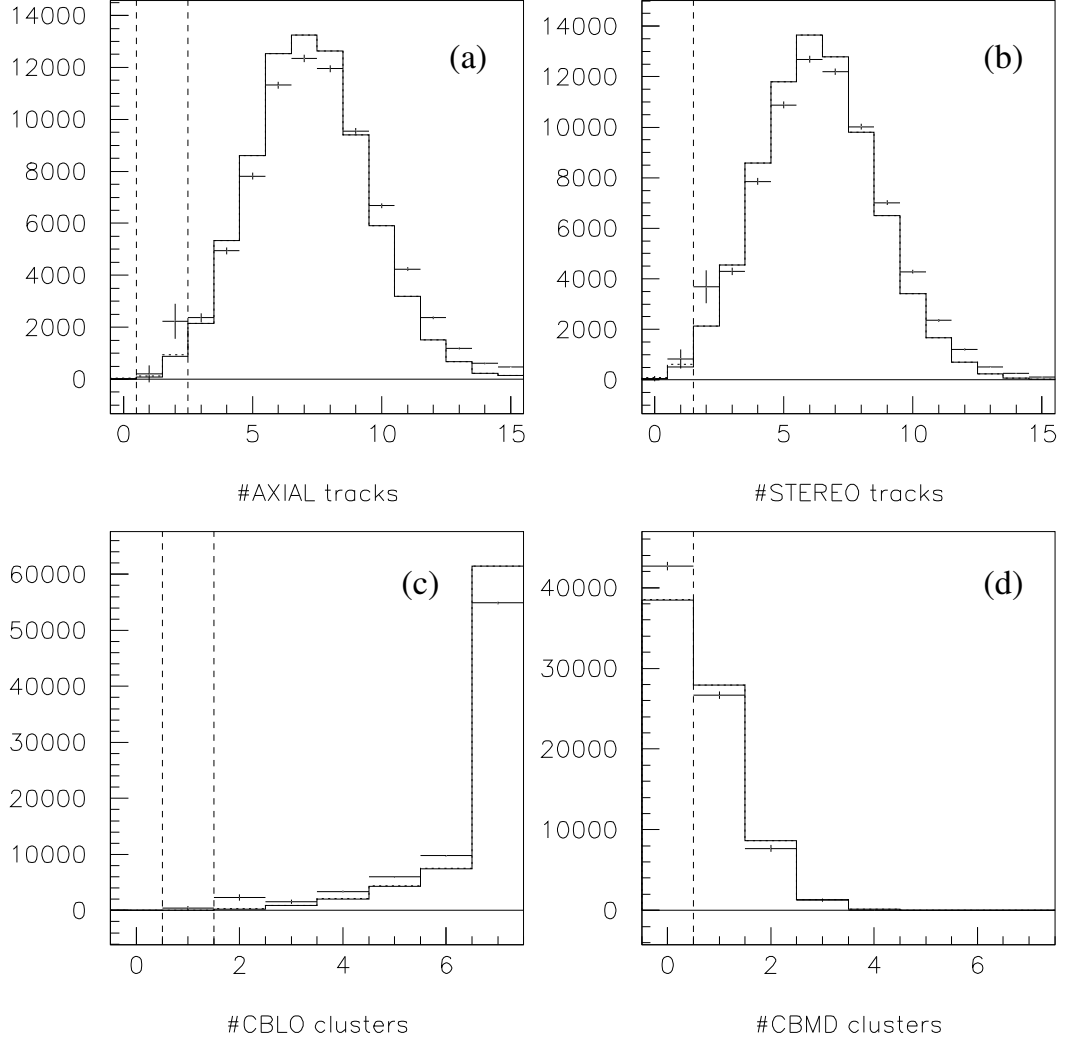


FIG. 9: Trigger variables as seen in hadronic data (points) and in Monte Carlo (histogram). (a) Number of AXIAL tracks, (b) STEREO tracks, (c) CBLO (150 MeV clusters), and (d) CBMD (750 MeV clusters). The analysis trigger decision is derived from these variables using Equation 3 (the lower limits are indicated by dotted lines). Data have been continuum-subtracted, cosmic-ray and beam-gas-subtracted, and the leptonic modes have been subtracted using Monte Carlo.

Efficiency of all modes except cascades to leptons (both $\Upsilon(2S)$ and $\Upsilon(3S)$)	$(97.35^{+0.58}_{-0.66})\%$
Efficiency of cascades to leptons from $\Upsilon(2S)$	$(0.69 \pm 0.22)\%$
Efficiency of cascades to leptons from $\Upsilon(3S)$	$(0.38 \pm 0.19)\%$
$\Upsilon(2S)$ cascade to leptons branching fraction	$(1.58 \pm 0.16)\%$
$\Upsilon(3S)$ cascade to leptons branching fraction	$(1.34 \pm 0.13)\%$
$\Upsilon(2S)$ hadronic efficiency (aggregate of the two components)	$(95.82^{+0.58}_{-0.66} \pm 0.15)\%$
$\Upsilon(3S)$ hadronic efficiency (aggregate of the two components)	$(96.05^{+0.58}_{-0.66} \pm 0.13)\%$

TABLE II: Summary of cut efficiency measurement for $\Upsilon(2S)$ and $\Upsilon(3S)$.

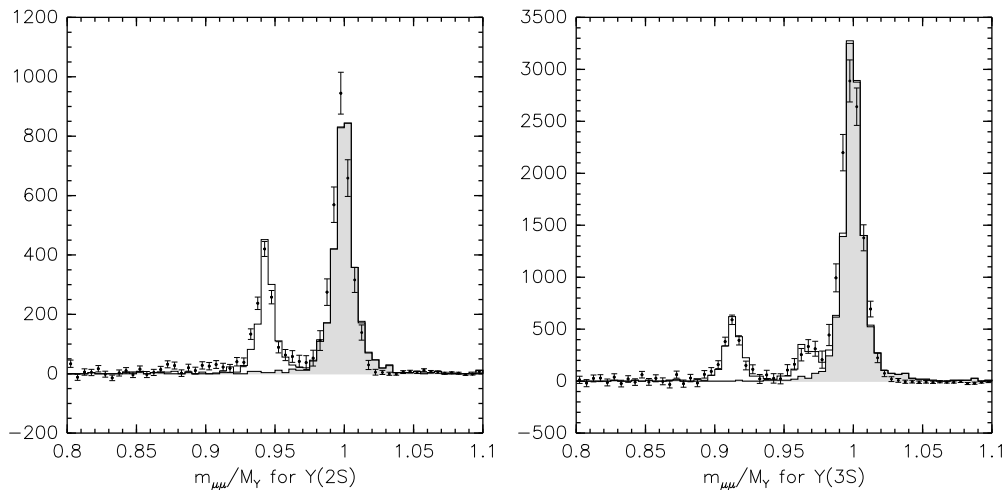


FIG. 10: Invariant mass of the two largest tracks (divided by M_Y) in $\Upsilon(2S)$ and $\Upsilon(3S)$ with Xe^+e^- rejected. Points are continuum-subtracted data, the shaded histogram is $\Upsilon(2S,3S) \rightarrow \mu^+\mu^-$ (prompt $\mu^+\mu^-$) Monte Carlo, and the empty histogram stacked on top of it is $\Upsilon(2S,3S) \rightarrow X\Upsilon \rightarrow X\mu^+\mu^-$ (cascade $\mu^+\mu^-$). The Monte Carlo normalizations have been fitted to the data, from which the cascade/prompt ratio is determined.

$\Upsilon(2,3S) \rightarrow \text{hadrons/taus}$ only predict a $(98.45 \pm 0.05)\%$ efficiency, to be compared with the $(98.68 \pm 0.04)\%$ $\Upsilon(1S)$ prediction above. The $\Upsilon(1S)$ efficiency is therefore corrected by 0.9977 ± 0.0007 , and this result, $(97.35^{+0.58}_{-0.66})\%$, is presented at the top of Table II.

The cascade to leptons mode, with two high-energy electrons or muons in the final state, is usually rejected by our largest track momentum cut: the efficiency is $(0.69 \pm 0.22)\%$ for $\Upsilon(2S)$ and $(0.38 \pm 0.19)\%$ for $\Upsilon(3S)$. We measured the branching fractions of $\Upsilon(2S)$ and $\Upsilon(3S)$ to this mode using our on- and off-resonance data. We select events with two high-momentum tracks ($> 70\%$ of beam energy), and reject those with a high-energy shower ($> 70\%$ of beam energy). After subtracting the appropriately-scaled continuum sample, we are left with a number of prompt $\mu^+\mu^-$ ($\Upsilon(2S,3S) \rightarrow \mu^+\mu^-$) and cascade $\mu^+\mu^-$ ($\Upsilon(2S,3S) \rightarrow X\Upsilon \rightarrow X\mu^+\mu^-$) events. These can be distinguished by the invariant mass of the $\mu^+\mu^-$ pair, as seen in Figure 10. We measure the ratio of cascade/prompt branching fractions by fitting the normalizations of cascade and prompt Monte Carlo to the data, and obtain the desired cascades to leptons branching fraction by multiplying by prompt $\mathcal{B}_{\mu\mu}$ (from [13])

$\times 2$. The Monte Carlo does not exactly reproduce the $\mu^+\mu^-$ invariant mass, which is the dominant uncertainty ($\lesssim 10\%$ of itself). The cascades to leptons branching fractions are $(1.58 \pm 0.16)\%$ for $\Upsilon(2S)$ and $(1.34 \pm 0.13)\%$ for $\Upsilon(3S)$.

The total hadronic efficiency is an aggregate of the cascade to leptons part and the non-cascade to leptons part, i.e.,

$$\begin{aligned}\epsilon_{MC}(2S) &= (0.0158) 0.69\% + (1 - 0.0158) 97.35\% = (95.82^{+0.58}_{-0.66} \pm 0.15)\% \\ \epsilon_{MC}(3S) &= (0.0134) 0.38\% + (1 - 0.0134) 97.35\% = (96.05^{+0.58}_{-0.66} \pm 0.13)\%.\end{aligned}$$

The first (asymmetric) uncertainty is common to all three resonances, while the second is from the cascade to leptons measurements, which dominates the efficiency differences.

C. Luminosity

For each beam energy, we can now count hadronic Υ decays, subtract non- Υ backgrounds from this count, and correct it for missing Υ events. All that remains is to remove the effects of variable run lengths by converting this number into a cross-section: we need to measure the integrated luminosity at each energy point. We have two concerns: the first is to determine the integrated luminosity of each measurement up to a single constant, so that observed lineshapes are undistorted. We will measure these “relative luminosities” by counting Gamgam events at each energy. The second concern is to determine the last constant, the absolute luminosity, turning a number of Gamgams into nb^{-1} and setting the scale for all three Γ_{ee} measurements.

Gamgam events ($e^+e^- \rightarrow \gamma\gamma$) have a distinct signature—two large, back-to-back showers—so backgrounds are not an issue above our level of consideration (0.1%). Also, we do not need to know the efficiency of our Gamgam cuts for a relative luminosity measurement. We require there to be no tracks in the drift chamber, two large ($> 70\%$ of beam energy) showers in the calorimeter which are back-to-back in ϕ (the polar angle around the beamline; we require $|\sin \phi_1 - \phi_2| < 0.04$ to avoid the nearly back-to-back showers from e^+e^-), and back-to-back in θ (the azimuthal angle; we require $|\cot \theta_1 + \cot \theta_2| < 0.1$, as the calorimeter has a barrel geometry and crystal elements are equally spaced in $\cot \theta$). We also restrict (θ_1, θ_2) to be far from the edge of the calorimeter barrel ($\min(|\cot \theta_1|, |\cot \theta_2|) < 1.18$ and $\max(|\cot \theta_1|, |\cot \theta_2|) < 1.28$) and far from the center ($\min(|\cot \theta_1|, |\cot \theta_2|) > 0.05$ and $\max(|\cot \theta_1|, |\cot \theta_2|) > 0.15$). At the edge, showers may be clipped, and at the center, the trigger is inefficient.

Since Gamgam events have no tracks, they rely on the back-to-back 1.5 GeV-cluster trigger. This trigger accepts events with two high-energy clusters which are moderately back-to-back in ϕ (our cut is much tighter) and on opposite sides of the detector in θ . Near the center, both photons may be found on the same side of the detector and the trigger is inefficient. We cut this region out. There are three other regions where the trigger is inefficient: some calorimeter trigger tiles were unresponsive for part of Υ data-taking. We also cut these regions out (for all data).

To convert these Gamgam counts into nb^{-1} , the integrated luminosity of all off-resonance data was measured to be 0.76 fb^{-1} with a fractional accuracy of 1.8%. This measurement used e^+e^- , $\gamma\gamma$, and $\mu^+\mu^-$ events, following the method of [11]; event counts were normalized with a Monte Carlo simulation based on the Babayaga [12] event generator. (The 1.8% systematic error reflects the agreement of the e^+e^- , $\gamma\gamma$, and $\mu^+\mu^-$ measurements: it is the

root mean square of their values around the mean.) By comparing the Gamgam count for off-resonance data with the Gamgam count for any other measurement, we obtain integrated luminosities which are not distorted by resonance effects and share a common uncertainty.

IV. CROSS-SECTION AND BEAM-ENERGY MEASUREMENT STABILITY

A. Cross-section Measurement Stability

We primarily use the drift chamber to count hadronic events and the calorimeter to count Gamgams, so the cross-section relies on these two detectors being synchronized. If one fails while the other continues to count, the measured cross-section will be too low or too high.

The calorimeter can fail to count a Gamgam event if one of the two photons enters a tile which isn't read out by the trigger. This is why we rejected these regions with our Gamgam cuts, to stabilize the count by making these regions always inefficient. We measure the Gamgam trigger efficiency by selecting Bhabhas with the drift chamber and asking how often the Gamgam trigger is satisfied by the two energetic electrons. For good runs, the Gamgam trigger is 99.7% efficient after cuts, with a $\sim 0.2\%$ statistical precision in each.

The drift chamber can fail if it loses high voltage and therefore sensitivity to all charged particles. We checked for drift chamber insensitivity by selecting Bhabhas with the calorimeter ($0.04 < |\sin \phi_1 - \phi_2| < 0.25$) and asking how often the drift chamber trigger failed to see one AXIAL track. In good runs, at most 0.3% of Bhabhas have no tracks (Gamgam might be a background).

A way to check the stability of the luminosity measurement is to compare Gamgam counts with Bhabha counts off-resonance, where the Υ background is minimal. The Gamgam/Bhabha ratio is 0.0793 ± 0.0002 , 0.0792 ± 0.0001 , and 0.0793 ± 0.0002 for the three measurements, all in statistical agreement and very precise (0.2%).

To put an upper limit on cross-section instability, we consider the consistency of all off-resonance runs at the same energy with a common cross-section measurement. The negative log likelihood of this agreement is

$$L(\delta_x) = \sum_{i=1}^{526} -\ln \left(\frac{1}{\sqrt{2\pi(\delta_{\sigma_i}^2 + \delta_x^2)}} \exp \left(-\frac{(\sigma_i - \langle \sigma \rangle)^2}{2(\delta_{\sigma_i}^2 + \delta_x^2)} \right) \right) \quad (5)$$

where $\sigma_i \pm \delta_{\sigma_i}$ are the individual cross-section measurements, $\langle \sigma \rangle$ is their mean (different below each resonance), and δ_x is a hypothetical fluctuation in cross-section beyond the statistical error. To raise $L(\delta_x)$ above $L(0)$ by 0.5, a δ_x of 0.03 nb is needed. This is smaller than the typical statistical error of 0.2 nb, and is derived from a larger dataset than the lineshape scans. An S -factor in analogy to the PDG's can't be used here, as $S(0) < 1$.

Fitting simulations with this small error indicate that it can change the value of Γ_{ee} by only 0.1%.

B. Beam-energy Measurement Stability

We minimized our sensitivity to fluctuations in the beam energy measurement by collecting data in small, independent scans, and by alternating measurements above and below

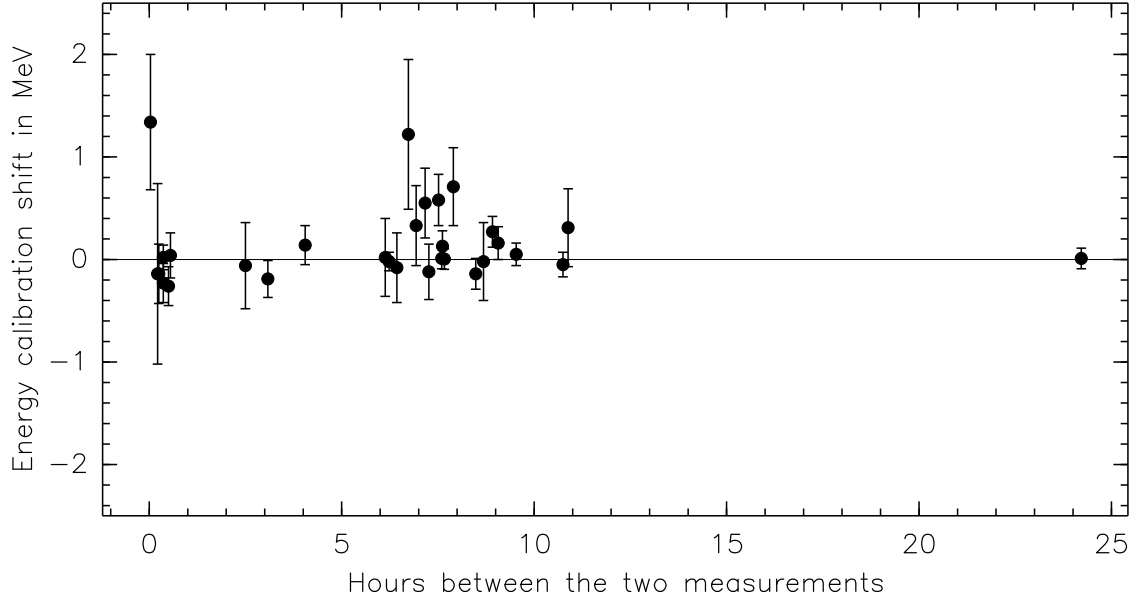


FIG. 11: Beam energy calibration shifts, as determined from thirty pairs of repeated cross-section measurements (plotted versus time).

the Υ mass. To determine the stability of this measurement, most weekly scans included two cross-section measurements at the same energy, usually near the beginning and end of the scan and at a point where the lineshape has a high derivative. If the beam energy calibration does not fluctuate between the two measurements, the hadronic cross-sections should be statistically consistent. If it fluctuates by a large amount, we would see a different hadronic cross-section, and can divide this difference by the derivative of the lineshape to measure the shift in beam energy calibration. If the beam energy fluctuates rapidly, many times during a single cross-section measurement, this contributes to the natural beam energy spread and is not relevant. Note that the calibration shifts under consideration here must take place during a weekly scan, not between them, as only these can distort the lineshape.

We converted thirty pairs of repeated measurements into beam energy calibration shifts, and plotted them in Figure 11 as a function of time between the end of the early and the beginning of the late measurement. As there is no evidence of any calibration shift, we construct an upper limit the same way we did for cross-section stability:

$$L(\delta_E) = \sum_{i=1}^{30} -\ln \left(\frac{1}{\sqrt{2\pi(\delta_{s_i}^2 + \delta_E^2)}} \exp \left(-s_i^2/2/(\delta_{s_i}^2 + \delta_E^2) \right) \right) \quad (6)$$

where $s_i \pm \delta_{s_i}$ are the calibration shift measurements plotted in Figure 11, and δ_E is an assumed uncertainty in beam energy. To raise $L(\delta_E)$ above $L(0)$ by 0.5, a δ_E of 0.05 MeV is needed. An S -factor in analogy to the PDG's would set δ_E at 0.07 MeV.

Fitting simulations with a δ_E of 0.05 MeV or 0.07 MeV indicate that it can change the value of Γ_{ee} by 0.2%.

	$\Upsilon(1S)$	$\Upsilon(2S)$	$\Upsilon(3S)$
$\chi^2/\text{\#degrees of freedom}$	$\frac{229.8}{210 - 15} = 1.18$	$\frac{57.6}{75 - 9} = 0.87$	$\frac{155.2}{175 - 10} = 0.94$
Confidence level	4%	76%	70%
$\int \sigma(e^+e^- \rightarrow \Upsilon \rightarrow \text{hadrons}) dE$ (in MeV nb)	318.9 ± 2.1	133.2 ± 2.1	84.9 ± 1.9
$\int \sigma(e^+e^- \rightarrow \Upsilon) dE$ (in MeV nb)	345.0 ± 2.4	141.9 ± 2.3	91.5 ± 2.0
Statistical uncertainty	0.7%	1.6%	2.2%

TABLE III: Fit results.

V. FITTING

For each resonance lineshape fit, the background level σ_b is allowed to float: the $1/s + \log s$ background shape is only extrapolated 50 MeV or so within an Υ lineshape. The Breit-Wigner area (Γ_{ee}) also floats, as does the beam energy spread ΔE . Also, the peak position of each weekly scan (12 for $\Upsilon(1S)$, 6 for $\Upsilon(2S)$, and 7 for $\Upsilon(3S)$) floats in the fit. By this, we mean that data from one week can slide up and down in beam energy independently of data from another week, while the theoretical lineshape is fixed at the known Υ mass.

The peak fit function is a convolution of a Breit-Wigner, a Gaussian, and an initial-state radiation tail, with an interference term between the Breit-Wigner and the continuum background. The Υ has a 10% branching fraction to $q\bar{q}$, and $e^+e^- \rightarrow q\bar{q}$ is the primary component of the continuum. In principle, the observed cross-section is not the sum of these two, but is proportional to the squared sum of their amplitudes:

$$\sigma(e^+e^- \rightarrow X \rightarrow q\bar{q}) \propto |\mathcal{M}(e^+e^- \rightarrow q\bar{q}) + \mathcal{M}(e^+e^- \rightarrow \Upsilon \rightarrow q\bar{q})|^2 \quad (7)$$

$$\propto |\mathcal{M}(e^+e^- \rightarrow q\bar{q})|^2 + |\mathcal{M}(e^+e^- \rightarrow \Upsilon \rightarrow q\bar{q})|^2 + 2 \operatorname{Re} \mathcal{M}(e^+e^- \rightarrow q\bar{q})^* \mathcal{M}(e^+e^- \rightarrow \Upsilon \rightarrow q\bar{q}). \quad (8)$$

The last term is the interference term, and it distorts the Υ lineshape by causing a deficit of events below the Υ mass and an excess above it. The data, however, are not statistically sensitive to this effect. (The interference term, at its maximum, is about a factor of 70 smaller than the peak at its maximum.)

As previously mentioned, 58% of $\Upsilon \rightarrow \tau^+\tau^-$ survive hadronic cuts, so these are added as a contribution to the fit function. These events have the same lineshape as the hadronic decays, except for an interference term which is larger by a factor of 10 relative to its peak (see the inset in Figure 3).

The background has the $1/s + \log s$ shape described in Section III A, plus tails from $\Upsilon(1S)$ and $\Upsilon(2S)$.

The $\Upsilon(1S)$, $\Upsilon(2S)$, and $\Upsilon(3S)$ lineshape fits are presented in Figure 12 with pull distributions in Figures 13, 14, and 15. Fit results are presented in Table III: the statistical uncertainties of 0.7%, 1.6%, and 2.2% are dominated by Gamgam counting. The $\Upsilon(1S)$ reduced χ^2 is moderately high (1.2, with a 4% C.L.), but a combined χ^2 of the three fits is $442.6/426 = 1.04$, with a 28% confidence level.

Systematic uncertainties from varying each fixed parameter are listed in Table IV, all of which are very small. The largest, theoretical error in the calculation of the high-energy tail, is shared by all three resonances.

	$\Upsilon(1S)$	$\Upsilon(2S)$	$\Upsilon(3S)$
From uncertainty in the full-width Γ	0.005%	0.02%	0.03%
Interference term for $q\bar{q}$ (depends on $\mathcal{B}_{\mu\mu}, R$)	0.02%	0.02%	0.002%
Interference term for $\tau^+\tau^-$ (depends on $\mathcal{B}_{\tau\tau}$)	0.08%	0.07%	0.05%
Two-photon fraction	0.002%	0.002%	0.001%
Initial-state radiation tail (0.1% theory error)	0.05%	0.05%	0.05%
Total (in quadrature)	0.05%	0.06%	0.05%

TABLE IV: Systematic uncertainties in the shape of the fit function.

VI. RESULTS AND DISCUSSION

Measured values of Γ_{ee} and all systematic uncertainties are listed in Table V (we consulted [13] for $\mathcal{B}_{\mu\mu}$). Ratios of Γ_{ee} (for which the luminosity calibration and some efficiency systematics cancel) are listed in Table VI, and $\Gamma_{ee}\Gamma_{\text{had}}/\Gamma_{\text{tot}}$ in Table VII ($\mathcal{B}_{\tau\tau}$ is from [14]). This last quantity does not have the leptonic modes added, so we did not introduce the assumption of Lepton Universality as we did for Γ_{ee} and its ratios.

These three di-electron widths, 1.343 ± 0.009 (*stat*) ± 0.026 (*syst*) keV, $0.620 \pm 0.010 \pm 0.012$ keV, and $0.427 \pm 0.009 \pm 0.009$ keV for the $\Upsilon(1S)$, $\Upsilon(2S)$, and $\Upsilon(3S)$ fix the full widths at 53.9 ± 1.9 keV, 30.5 ± 1.5 keV, and 17.9 ± 1.1 keV, assuming $\mathcal{B}_{ee} = \mathcal{B}_{\mu\mu}$ [13]. These imply Υ lifetimes of $(12.2 \pm 0.4) \times 10^{-21}$ s, $(21.6 \pm 1.1) \times 10^{-21}$ s, and $(36.8 \pm 2.3) \times 10^{-21}$ s.

We can also apply Equation 1 to learn that $|\psi(0, 0, 0)|^2 = 17.5 \pm 0.4 \text{ fm}^{-3}$, $9.1 \pm 0.2 \text{ fm}^{-3}$, and $6.7 \pm 0.2 \text{ fm}^{-3}$ for the $\Upsilon(1S)$, $\Upsilon(2S)$, and $\Upsilon(3S)$ respectively. (Warning: Equation 1 was derived assuming purely non-relativistic quarks, which is only approximately true for b quarks in Υ resonances. Relativistic corrections can increase $|\psi(0, 0, 0)|^2$.) To get a rough idea of how large these three resonances are in space, we can approximate the $b\bar{b}$ potential with a Coulomb potential and derive an RMS spread of 0.2 fm, 1.4 fm, and 4 fm for the three resonances, respectively. The real potential rises much more rapidly at large quark spacings than a Coulomb potential, so we can presume that the three states differ in width by less than the factor of 20 calculated above. These kinds of questions can be much better treated in the context of lattice QCD, which this experiment will hopefully verify.

VII. ACKNOWLEDGEMENTS

We gratefully acknowledge the effort of the CESR staff in providing us with excellent running conditions. We also would like to thank Istvan Danko and Surik Mehrabyan for helpful discussions at all stages of the analysis, as well as Christine Davies and Peter Lepage for help in understanding the theoretical calculation that motivated this measurement.

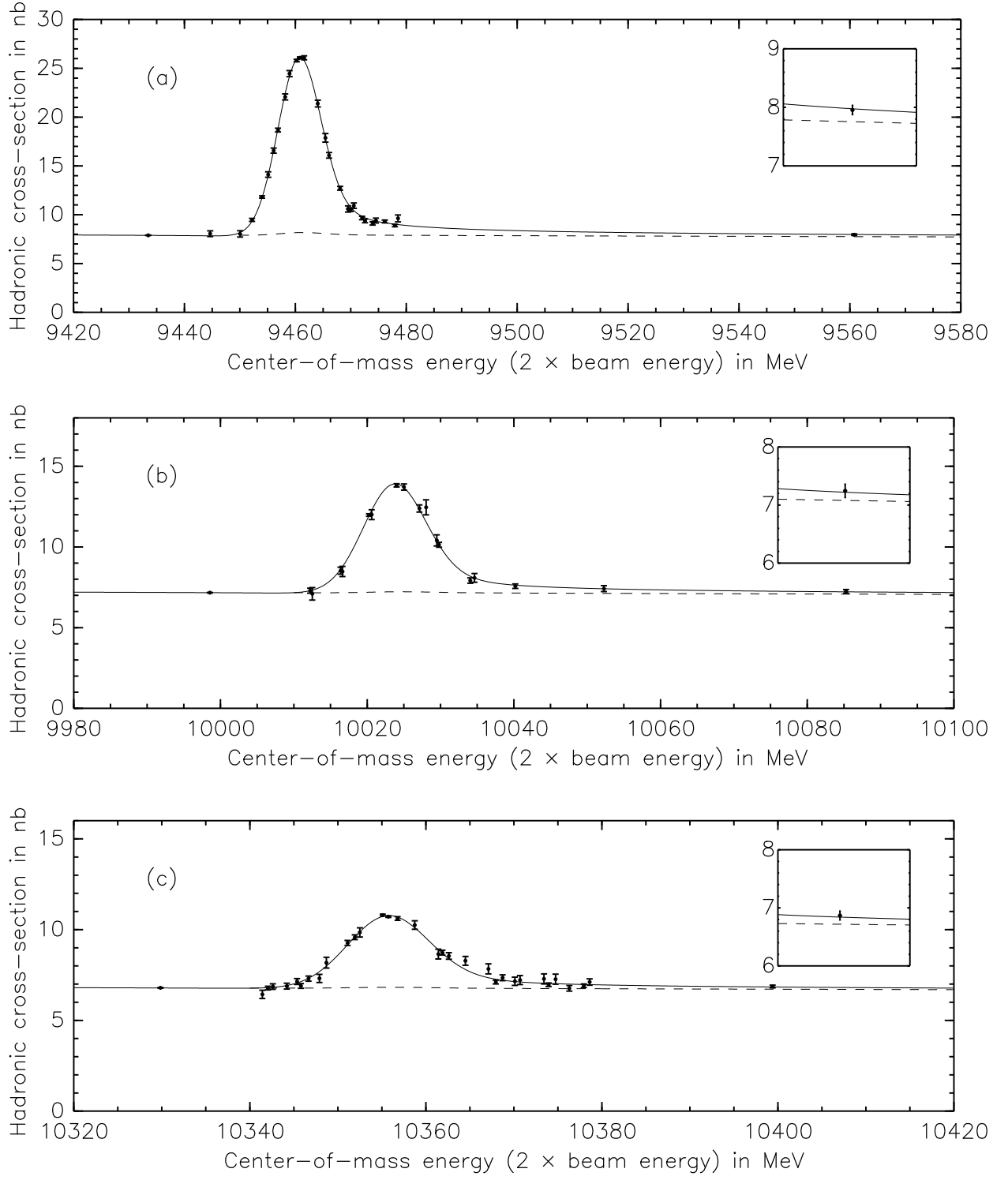


FIG. 12: Best-fit to the (a) $\Upsilon(1S)$ lineshape, (b) $\Upsilon(2S)$ lineshape, and (c) $\Upsilon(3S)$ lineshape. Measurements at the same beam energy have been combined in this plot, but not in the fit (only the off-resonance and high-energy tail points were combined in the fit). The dashed line is the sum of all backgrounds (including $\Upsilon \rightarrow \tau^+\tau^-$), and the inset shows a close-up of the high-energy tail.

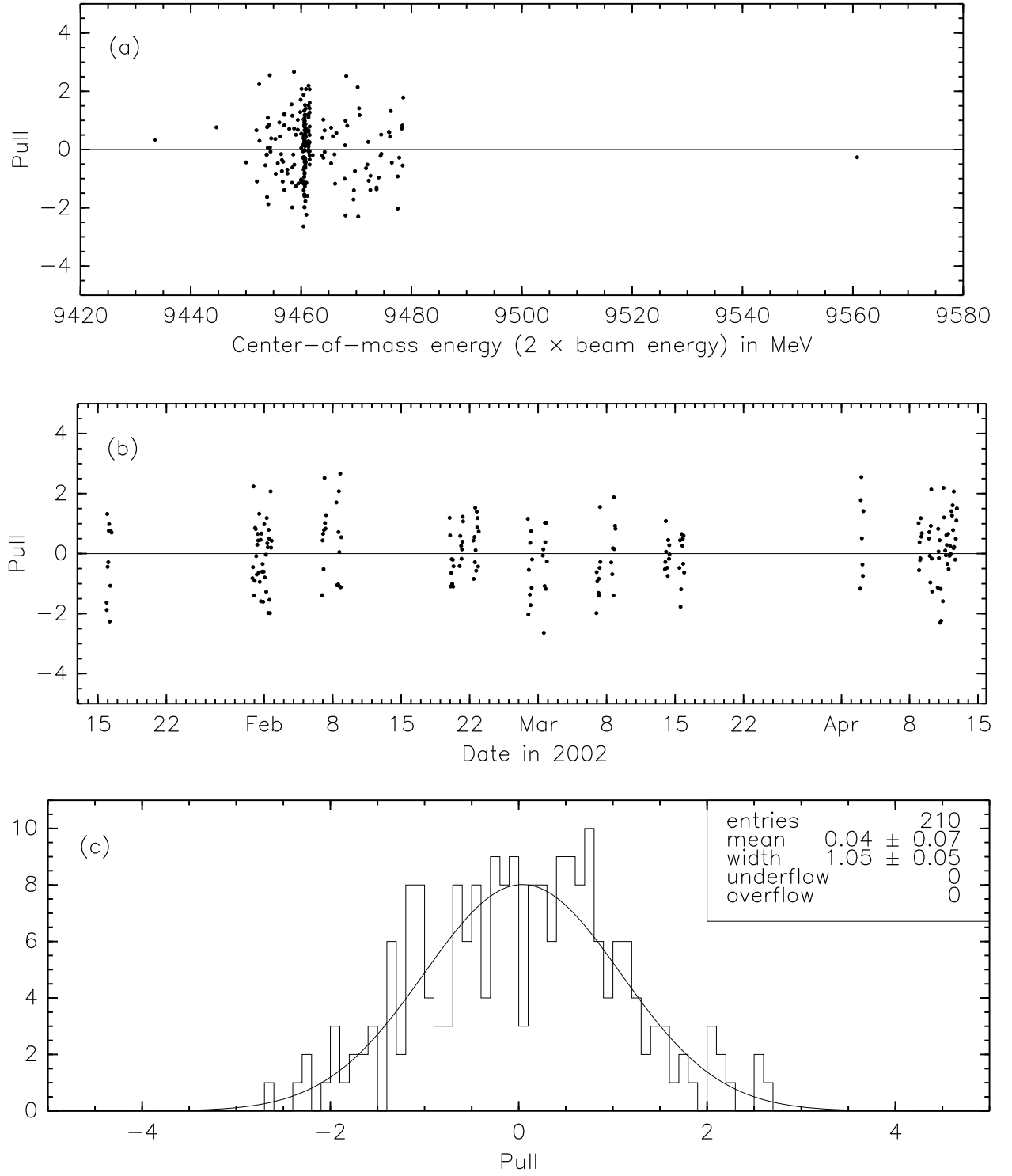


FIG. 13: Pull distributions ($(\text{observed} - \text{fit})/\text{uncertainty}$) for the $\Upsilon(1S)$ fit: (a) versus energy, (b) versus date of measurement, and (c) as a histogram.

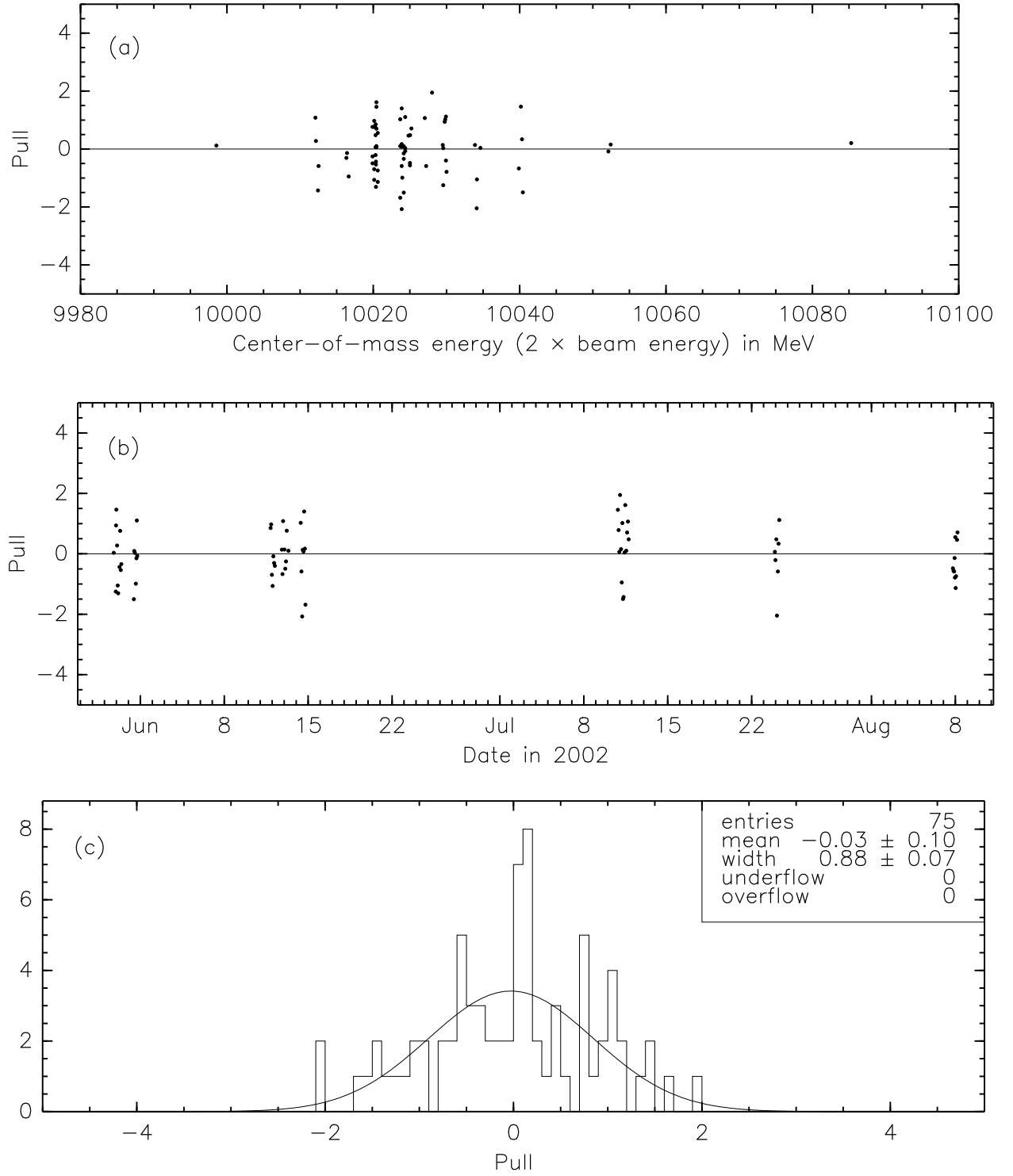


FIG. 14: Pull distributions $((\text{observed} - \text{fit})/\text{uncertainty})$ for the $\Upsilon(2S)$ fit: (a) versus energy, (b) versus date of measurement, and (c) as a histogram.

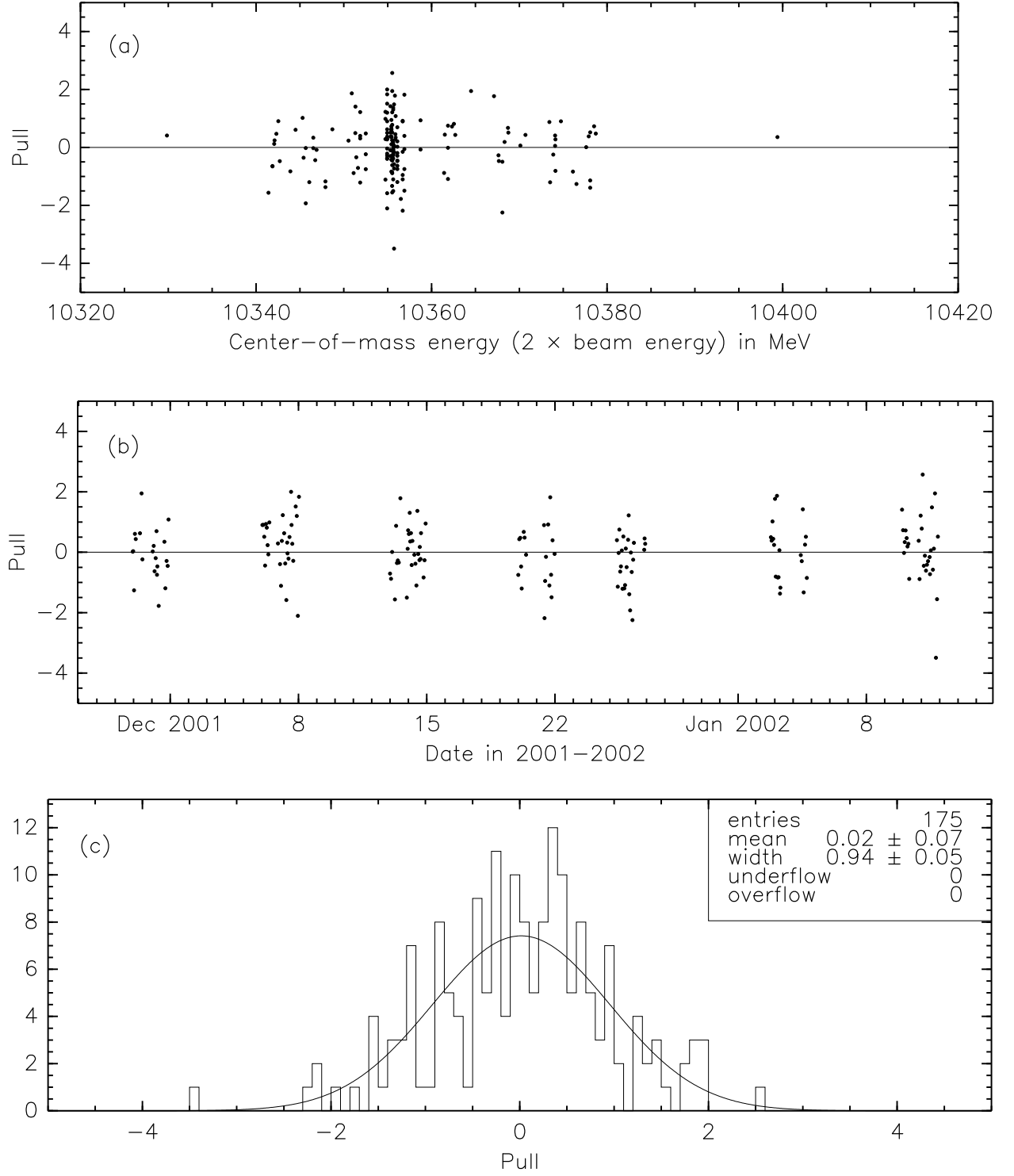


FIG. 15: Pull distributions $((\text{observed} - \text{fit})/\text{uncertainty})$ for the $\Upsilon(3S)$ fit: (a) versus energy, (b) versus date of measurement, and (c) as a histogram.

Contribution to Γ_{ee}	$\Upsilon(1S)$	$\Upsilon(2S)$	$\Upsilon(3S)$
Statistical (Table III)	0.7%	1.6%	2.2%
Hadronic efficiency (Tables I and II)	0.7%	0.7%	0.7%
$(1 - 3\mathcal{B}_{\mu\mu})$ ($\mathcal{B}_{\mu\mu}$ is from [13])	0.2%	0.2%	0.3%
Luminosity calibration (Page 15)	1.3%	1.3%	1.3%
Shape of the fit function (Table IV)	0.05%	0.06%	0.05%
Cross-section stability (Section IV A)	0.1%	0.1%	0.1%
Beam-energy stability (Section IV B)	0.2%	0.2%	0.2%
Result (in keV $\pm stat \pm syst$)	$0.618 \pm 0.010 \pm 0.009$		
	$1.339 \pm 0.009 \pm 0.020$		$0.425 \pm 0.009 \pm 0.006$
Fractional uncertainty	1.7%	2.2%	2.7%

TABLE V: Values and uncertainties in Γ_{ee} .

Contribution to ratio of Γ_{ee}	$\Upsilon(2S)/\Upsilon(1S)$	$\Upsilon(3S)/\Upsilon(1S)$	$\Upsilon(3S)/\Upsilon(2S)$
Statistical	1.7%	2.3%	2.7%
Hadronic efficiency	0.15%	0.13%	0.20%
$(1 - 3\mathcal{B}_{\mu\mu})$	0.3%	0.4%	0.4%
Luminosity calibration	0	0	0
Shape of the fit function	0.11%	0.10%	0.10%
Cross-section stability	0.14%	0.14%	0.14%
Beam-energy stability	0.3%	0.3%	0.3%
Result ($\pm stat \pm syst$)	$0.317 \pm 0.007 \pm 0.002$		
	$0.462 \pm 0.008 \pm 0.002$		$0.688 \pm 0.019 \pm 0.004$
Fractional uncertainty	1.8%	2.4%	2.8%

TABLE VI: Values and uncertainties in ratios of Γ_{ee} .

Contribution to $\Gamma_{ee}\Gamma_{\text{had}}/\Gamma_{\text{tot}}$	$\Upsilon(1S)$	$\Upsilon(2S)$	$\Upsilon(3S)$
Statistical	0.7%	1.6%	2.2%
Hadronic efficiency	0.7%	0.7%	0.7%
Uncertainty in $\mathcal{B}_{\tau\tau}$ ($\mathcal{B}_{\tau\tau}$ is from [14])	0.09%	0.19%	0.16%
Luminosity calibration	1.3%	1.3%	1.3%
Shape of the fit function	0.05%	0.06%	0.05%
Cross-section stability	0.1%	0.1%	0.1%
Beam-energy stability	0.2%	0.2%	0.2%
Result (in keV $\pm stat \pm syst$)	$0.580 \pm 0.009 \pm 0.009$		
	$1.238 \pm 0.009 \pm 0.019$		$0.395 \pm 0.009 \pm 0.006$
Fractional uncertainty	1.7%	2.2%	2.7%

TABLE VII: Values and uncertainties in $\Gamma_{ee}\Gamma_{\text{had}}/\Gamma_{\text{tot}}$. We have not assumed Lepton Universality in this Table.

-
- [1] M. E. Peskin and D. V. Schroeder, *An Introduction to quantum field theory*. Reading, USA: Addison-Wesley (1995) 842 p.
 - [2] C.T.H. Davies *et al.*, Phys. Rev. Lett. **92**, 022001 (2004)
 - [3] S. Eidelman *et al.*, Phys. Lett. B **592**, 1 (2004)
 - [4] E.A. Kuraev and V.S. Fadin, Sov. J. Nucl. Phys. **41**, 466 (1985).
 - [5] K. Berkelman, *Primer on Onium Widths*, CBX 02-10, and *Onium Line Shape Fitting*, CBX 03-12.
 - [6] CLEO Collaboration, CLNS-94-1277; D. Peterson *et al.*, Nucl. Instr. and Meth. A **478**, 142 (2002)
 - [7] S. Agostinelli *et al.*, Nucl. Instr. and Meth. A **506**, 250 (2003)
 - [8] D.J. Lange Nucl. Instr. and Meth. A **462**, 152 (2001)
 - [9] T. Sjöstrand, Comput. Phys. Commun. **82**, 74 (1994).
 - [10] Inga Karliner, private communication.
 - [11] G. Crawford *et al.* (CLEO Collaboration), Nucl. Instrum. Methods Phys. Res., Sect. A **345**, 429 (1992).
 - [12] C.M. Carloni Calame *et al.*, Nucl. Phys. Proc. Suppl. B **131**, 48 (2004).
 - [13] G.S. Adams *et al.*, Phys. Rev. Lett. **94**, 012001 (2005)
 - [14] J.E. Duboscq, *First Observation of $\Upsilon(3S) \rightarrow \tau\tau$ and Precision Measurement of $B(\Upsilon(2S) \rightarrow \tau\tau)$ and $B(\Upsilon(1S) \rightarrow \tau\tau)$* , CBX 05-30.